nature chemistry

ARTICLES

https://doi.org/10.1038/s41557-022-00995-0

Check for updates

OPEN

A general design of caging-group-free photoactivatable fluorophores for live-cell nanoscopy

Richard Lincoln[1,4], Mariano L. Bossi[2,4], Michael Remmel[1], Elisa D'Este[3], Alexey N. Butkevich[1]✉ and Stefan W. Hell[1,2]✉

The controlled switching of fluorophores between non-fluorescent and fluorescent states is central to every super-resolution fluorescence microscopy (nanoscopy) technique, and the exploration of radically new switching mechanisms remains critical to boosting the performance of established, as well as emerging super-resolution methods. Photoactivatable dyes offer substantial improvements to many of these techniques, but often rely on photolabile protecting groups that limit their applications. Here we describe a general method to transform 3,6-diaminoxanthones into caging-group-free photoactivatable fluorophores. These photoactivatable xanthones (PaX) assemble rapidly and cleanly into highly fluorescent, photo- and chemically stable pyronine dyes upon irradiation with light. The strategy is extendable to carbon- and silicon-bridged xanthone analogues, yielding a family of photoactivatable labels spanning much of the visible spectrum. Our results demonstrate the versatility and utility of PaX dyes in fixed and live-cell labelling for conventional microscopy, as well as the coordinate-stochastic and deterministic nanoscopies STED, PALM and MINFLUX.

Fluorescence nanoscopy has revolutionized our ability to visualize (living) cells by extending the limits of optical imaging to single-digit nanometre resolution, and by enabling minimally invasive observation of the internal nanoscale structures and dynamics of biological samples with molecular specificity[1–4]. Central to these techniques are chemically specific fluorescent labels and the intrinsic control between fluorescent (on) and non-fluorescent (off) states of the fluorophores. This sequential off–on transition is key to separating adjacent fluorophores at molecule-scale proximities. Photoactivatable or caged dyes—in which the off–on transition is irreversible and triggered by light—render these nanoscopy techniques very powerful, because they eliminate the need for specific imaging buffers and high intensities of UV light. Such requirements are prevalent in single-molecule-based microscopy, such as photo-activated localization microscopy (PALM) or stochastic optical reconstruction microscopy (STORM), to drive commonly used fluorophores (for example, cyanines) between non-fluorescent and fluorescent states[5–7], as well as enabling high-density single-particle tracking[8–10]. Most recently, photoactivatable dyes have been used to reduce the fluorescence background in DNA-PAINT[11] and to increase the number of cellular structures that may be simultaneously imaged in stimulated emission depletion (STED) microscopy through channel duplexing[12].

Rhodamine dyes have emerged as some of the most widely employed fluorophores in fluorescence microscopy and nanoscopy due to the remarkable tunability of their optical and chemical properties[13–15], cell membrane permeability[16], photostability[17] and brightness[18]. In particular, silicon rhodamines[19] are often favoured for their intrinsic redshifted emission, fluorogenic behaviour[20] and live-cell compatibility[21–23]. However, the reported caging strategies for rhodamines rely on 'locking' the dyes in a non-fluorescent form, either through installation of photolabile protecting groups on the nitrogen atoms (such as with nitroveratryloxycarbonyl[7,24,25] or nitroso[26] groups) or by synthetic transformation of the lactone ring into the corresponding cyclic α-diazoketones[9,27]. The former strategy restricts the attainable substitution patterns, reduces water solubility and yields stoichiometric amounts of potentially toxic by-products upon photoactivation. The latter strategy, meanwhile, suffers from varying uncaging efficiencies and the concomitant formation of non-fluorescent side products, whose abundance depends on the medium and substitution pattern[27,28].

Accordingly, caging-group-free, compact photoactivatable and biocompatible fluorophores are highly desirable in fluorescence microscopy and nanoscopy applications, enabling lower-molecular-weight labels, provided that the photoactivation is rapid, complete and free of by-products. Recently, the photoactivation of a Si-pyronine analogue was demonstrated, where the fluorophore was initially masked with an exocyclic double bond at the 9-position of the Si-xanthene scaffold[29]. Upon UV irradiation in aqueous solution, protonation of the exocyclic double bond yielded the fluorescent 9-alkyl-Si-pyronine. The resulting cationic fluorophore, however, was susceptible to formation of non-fluorescent nucleophilic addition products with thiols and water, limiting its applicability.

Inspired by the long-established radical photochemistry of benzophenone and other diarylketones, we have now designed, and report herein, a class of functionalized xanthones, which, upon one- or two-photon excitation, convert efficiently and cleanly into the corresponding dihydropyran-fused pyronine dyes. These photoactivatable xanthone (PaX) dyes can be prepared from readily available starting materials via a straightforward and efficient three-step synthetic route, also compatible with carbon- and silicon-bridged

[1]Department of Optical Nanoscopy, Max Planck Institute for Medical Research, Heidelberg, Germany. [2]Department of NanoBiophotonics, Max Planck Institute for Multidisciplinary Sciences, Göttingen, Germany. [3]Optical Microscopy Facility, Max Planck Institute for Medical Research, Heidelberg, Germany. [4]These authors contributed equally: Richard Lincoln, Mariano L. Bossi. ✉e-mail: alexey.butkevich@mr.mpg.de; stefan.hell@mpinat.mpg.de

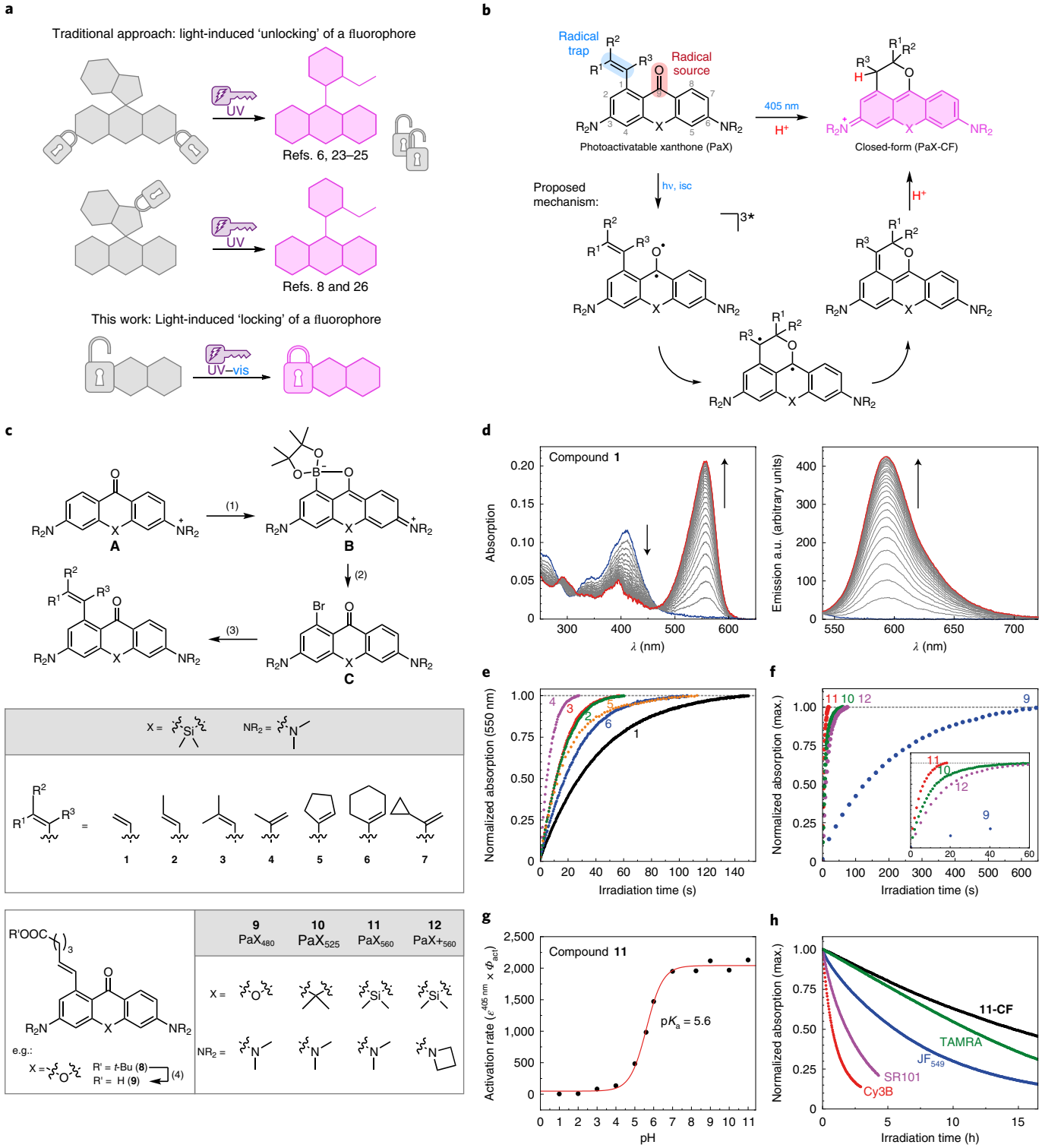

Fig. 1 | Design, synthesis and characterization of PaX dyes. a, Whereas traditional strategies for photoactivatable dyes for nanoscopy rely on the release ('unlocking') of caging groups, our approach relies on the light-induced assembly ('locking') of a fluorophore. **b**, General structure of a PaX with a 1-alkenyl radical trap and its 9-alkoxypyronine photoproduct (closed-form, **CF**), and the proposed photoactivation mechanism. **c**, Synthetic route for the preparation of PaX. (1) B_2pin_2, $[Ir(cod)(OMe)]_2$, $AsPh_3$, *n*-octane, 120 °C, 22 h; (2) $CuBr_2$, KF, pyridine, DMSO/H_2O, 80 °C, 30 min; (3) $RB(OH)_2$, RBpin or RBF_3K (R = alkenyl), $Pd(dppf)Cl_2$, K_2CO_3, dioxane/H_2O, 80 °C, 3–18 h; (4) CH_2Cl_2/TFA 3:1, r.t., 1 h. **d**, Temporal evolution of the absorption and fluorescence spectra of **1** (1.66 μg ml^{-1}) irradiated in phosphate buffer (100 mM, pH 7; λ_{act} = 405 nm). **e**, Comparative photoactivation kinetics of Si-bridged PaX **1**–**6**, under the same conditions as in **d**. **f**, Comparative photoactivation kinetics of PaX dyes **9**–**12**, under the same conditions as in **d**. Inset: magnified view of the 0–60 s time region. **g**, Comparative photoactivation kinetics of **11** (3.8 μM) in phosphate buffer (100 mM) at different pH values (λ_{act} = 405 nm). **h**, Photo-fatigue resistance of **11-CF** and established commercial fluorophores, with similar spectral properties, measured in phosphate buffer (λ_{exc} = 530 nm).

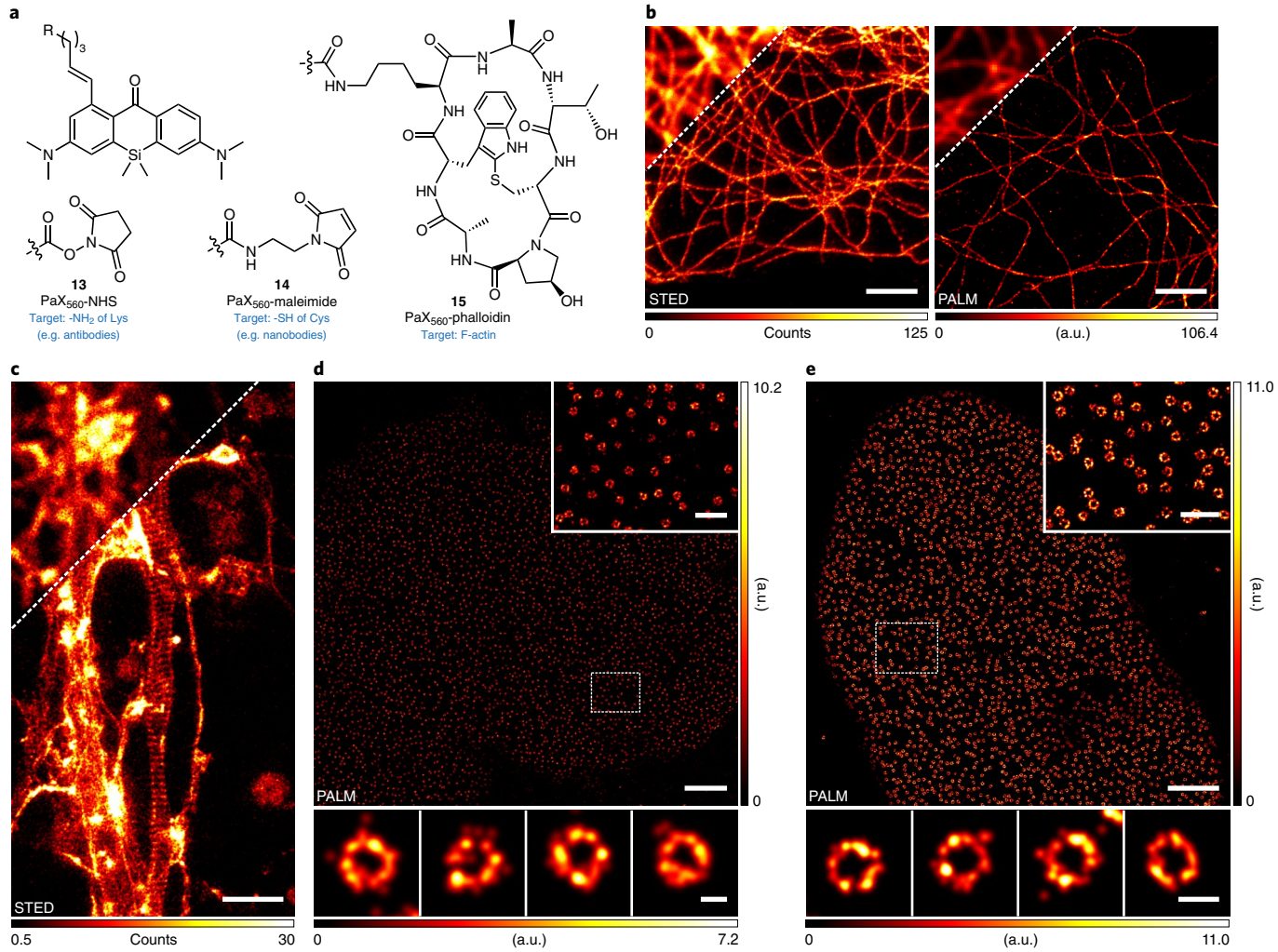

Fig. 2 | Photoactivatable labels for optical nanoscopy. a, Structures of PaX_{560} derivatives for bioconjugation (**13**, **14**) and actin labelling (**15**). **b**, STED (left) and PALM (right) images of microtubules in COS-7 cells labelled by indirect immunofluorescence with a secondary antibody bearing **13**. Preactivation to **13-CF** for STED imaging was achieved with widefield illumination (AHF analysentechnik AG, 4,6-diamidino-2-phenylindole filter set F46-816). **c**, Actin structures of the periodic membrane cytoskeleton in the axon of fixed primary hippocampal neuron cultures labelled with **15** and mounted in Mowiol. Preactivation to **15-CF** for STED imaging was achieved with widefield illumination (AHF, enhanced green fluorescent protein (EGFP) filter set F46-002) followed by a 518-nm laser. Image data were smoothed with a 1-pixel low-pass Gaussian filter. **d**, PALM image of NPCs in COS-7 cells labelled via indirect immunofluorescence with an anti-NUP98 primary antibody and a secondary nanobody labelled with **14**. Inset: magnified view of the region marked in the overview image. Bottom row: individual NPCs. **e**, PALM image of NPCs in HeLa-Kyoto cells expressing NUP107-mEGFP labelled with anti-GFP nanobodies conjugated to **14**. Inset: magnified view of the region marked in the overview image. Bottom row: individual NPCs. Scale bars: 2 μm (**b**–**e**, main images), 500 nm (**d**,**e** insets), 50 nm (**d**, bottom row), 100 nm (**e**, bottom row).

analogues, to yield a family of fluorophores spanning much of the visible spectrum. In particular, PaX-derived Si-pyronine dyes display good live-cell compatibility, resilience to nucleophiles, and an unprecedented photostability for orange-emitting (TAMRA-like) fluorophores. We highlight the utility of PaX dyes and labels in optical microscopy and nanoscopy techniques, in fixed and living cells, including STED, photo-activated localization microscopy (PALM) and minimal photon fluxes (MINFLUX).

Results and discussion

Synthetic design and proposed mechanism of photoactivation. In our search for minimalistic photoactivatable fluorophores, we reasoned that the concept of employing photochemical reactions to assemble or 'lock' fluorophores, rather than 'unlocking' photocleavable caging elements, would provide an improved alternative to caged rhodamine dyes (Fig. 1a)—a strategy similar to photochromic diarylethenes[30]. Diarylketones are known photoinitiators of radical reactions[31] due to their high inherent rate of intersystem crossing (via spin–orbit coupling) and their triplet states with diradical character[32,33]. We hypothesized that their photochemistry would be extendable to 3,6-diaminoxanthones, which are utilized as precursors in the synthesis of rhodamines[34–36]. With the introduction of a suitable intramolecular radical trap onto the xanthone scaffold, a juxtaposition of a radical source (diaryl ketone) and a radical trap (styrene) could be exploited to photoassemble 9-alkoxypyronine fluorophores through a light-triggered cascade (Fig. 1b)[37].

To investigate the effects of substitution of the radical acceptor, we first synthesized a series of photoactivatable Si-xanthones (**1**–**7**; Fig. 1c). The target compounds were prepared by an Ir-catalysed, chelation-assisted, *ortho*-selective C–H borylation of the diaryl ketone (**A**)[38]. Conversion of the resulting boronate ester (**B**) into the corresponding aryl bromide (**C**) was carried out with a

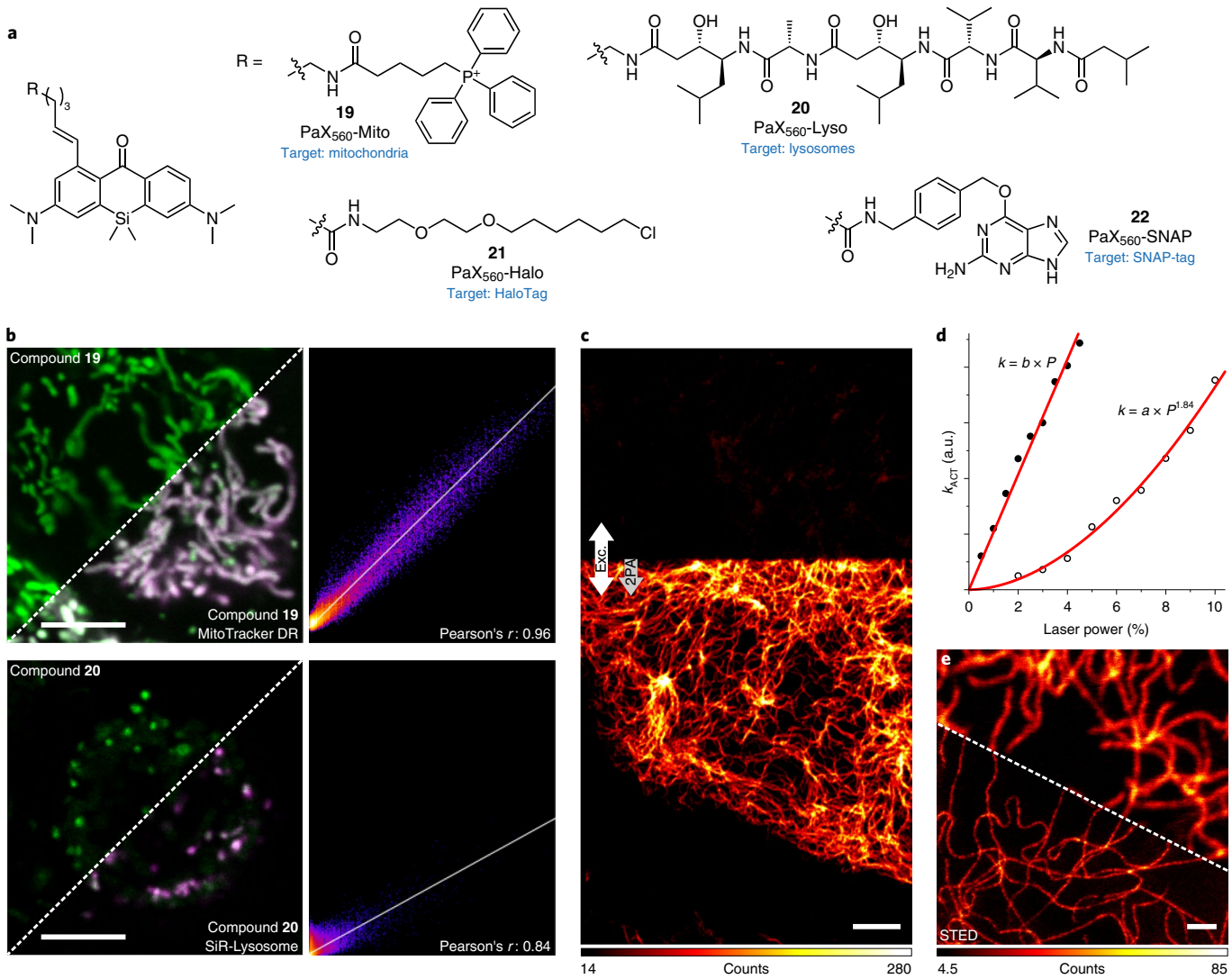

Fig. 3 | Imaging with photoactivatable PaX labels in living cells. a, Structures of PaX_{560} derivatives (**19**–**22**) for live-cell imaging. **b**, Confocal images and corresponding Pearson correlation analysis of COS-7 cells co-incubated with **19** (200 nM) and MitoTracker Deep Red (50 nM, top row) or **20** (20 nM) and SiR-lysosome (200 nM, bottom row). Conversion to **19-CF** and **20-CF** was achieved with a 355-nm laser. **c**, Confocal image of vimentin filaments labelled with **21** (200 nM) in U2OS cells before activation (upper portion) and with two-photon activation (2PA) (lower portion, indicated by the arrows). **d**, Plot of activation rate versus laser power for a one-photon (355 nm, 0.3 μW at 100%) or two-photon activation laser (810 nm, 109 mW at 10%). The lines represent fits of activation rate k_{ACT} to a linear or quadratic function of power P for one- or two-photon activation with parameters b and a, respectively. **e**, Confocal (top) and STED (bottom) images of the same sample following activation by a 405-nm laser. Scale bars: 5 μm (**b**,**c**) and 1 μm (**e**).

$CuBr_2$–pyridine system[39] in the presence of KF (details are provided in the Supplementary Information). A series of alkene substituents were then installed using standard Suzuki–Miyaura cross-coupling reaction conditions. Compounds **1**–**6** showed a strong absorption band ($\varepsilon \approx 10^4\,M^{-1}\,cm^{-1}$) at ~400 nm, characteristic of Michler's ketone and its analogues (Supplementary Table 1 presents the photophysical characterization). Upon irradiation in protic media (for example, phosphate buffer, 100 mM, pH 7), compounds **1**–**6** underwent rapid and complete conversion to give highly fluorescent 'closed-form' (CF) products with TAMRA-like spectral properties (**1-CF** to **6-CF**; Fig. 1d and Supplementary Fig. 1). Liquid chromatography mass spectrometry (LC-MS) analysis of the reaction mixtures revealed no by-products for most samples. The measured quantum yields of photoactivation (Φ_{PA}) ranged from 1×10^{-2} to 6×10^{-2} (Supplementary Table 1). The rate of photoactivation was slowest for vinyl-substituted compound **1**, increased with additional substitution of the alkene, and was highest for compound **4**, possibly due to a favourable orientation of the alkene induced by the α-methyl substituent (Fig. 1e). To confirm the formation of predicted 9-alkoxypyronine product **1-CF**, a solution of compound **1** in methanol was irradiated with a 405-nm light-emitting diode (LED) in a batch photoreactor (see Supplementary Information for details), and the resulting product was isolated and fully characterized by NMR and high-resolution mass spectrometry (HR-MS) analysis (Supplementary Fig. 2), confirming the expected dihydropyran ring fusion. A solvent-dependent protonation step was confirmed by conducting photolysis in methanol-d_4 (resulting in deuterium incorporation at the benzylic position) and by the absence of efficient photoactivation in aprotic solvents such as 1,4-dioxane. Deoxygenating the solvent increased the rate of photoactivation, confirming the role of the xanthone triplet state. Photolysis of **1** (4.8 μM) in the presence of millimolar concentrations of the radical trap 4-hydroxy-TEMPO resulted in the formation of a PaX-TEMPO adduct (Supplementary Fig. 3); however, the radical clock probe **7**

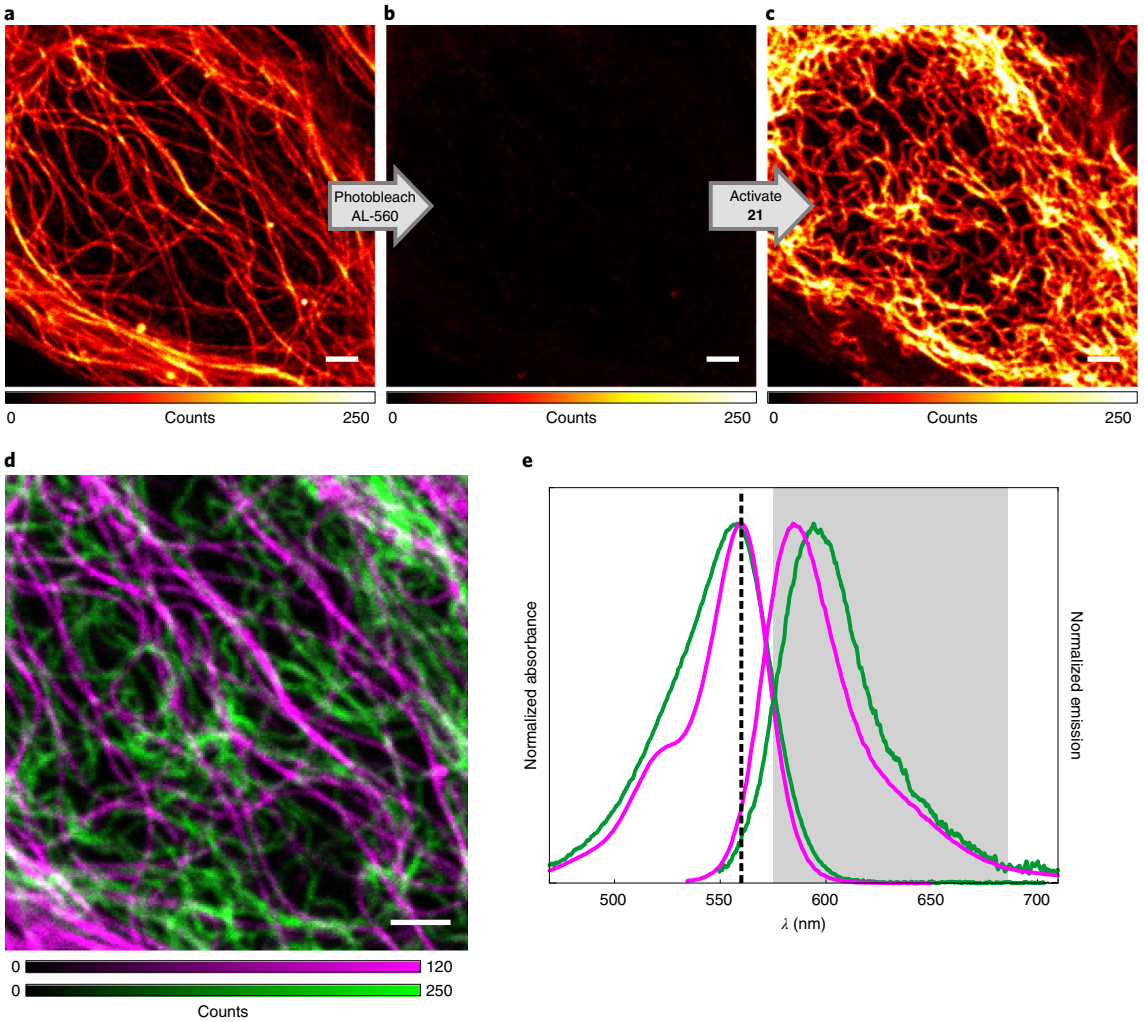

Fig. 4 | Channel duplexing with PaX labels. a–c, Confocal imaging of U2OS cells labelled with Abberior LIVE 560 tubulin (AL-560, 500 nM) and vimentin filaments labelled with compound **21** (100 nM) before (**a**) and after (**b**) photobleaching of AL-560 and after photoactivation by a 405-nm laser of **21** (**c**). **d**, Combined pseudo two-colour image showing tubulin (magenta) and vimentin (green) filaments obtained by sequential imaging (**a–c**). **e**, Absorption and emission spectra of AL-560 (magenta) and **21-CF** (green), with the excitation laser (dashed line) and detection window (grey) indicated. Scale bars, 2 µm (**a–d**).

showed no evidence of cyclopropane ring-opening upon photoactivation (Supplementary Fig. 4).

To render the PaX dyes suitable for bioconjugation, xanthone **9** (PaX_{480}), anthrone **10** (PaX_{525}) and Si-xanthone **11** (PaX_{560}), along with its bis-azetidine analogue **12** ($PaX+_{560}$), were prepared (Fig. 1c) bearing alkenyl substituents with a short carboxylate-terminated spacer. The keto forms of **9**, **10** and **11** showed initial absorbance maxima at 399, 408 and 414 nm, respectively (Supplementary Fig. 5 and Supplementary Table 2). The rate of photoactivation yielding the pyronine dyes (with absorption/emission maxima at 480/514 nm for **9-CF**, 524/564 nm for **10-CF** and 558/596 nm for **11-CF**) decreased in the order **11** > **10** > **9** (Fig. 1f), without noticeable by-product formation by LC-MS analysis, and the closed forms remained stable for at least 1 h at pH 7 (Supplementary Fig 6). As we expected, the azetidine auxochromic groups had little impact on the spectral properties of both the Si-xanthone (**12**) and Si-pyronine (**12-CF**) forms, but instead reduced the rate of photoactivation compared to the bis(*N*,*N*-dimethylamino) analogue (**11**). Fluorophore **12-CF** demonstrated remarkably improved emission quantum efficiency (0.92 versus 0.48 for **11-CF**), which can be attributed to the suppression of transfer into a twisted internal charge transfer state upon excitation[18].

Screening the photoactivation properties of **11** over a range of biologically relevant pH values (Fig. 1g and Supplementary Fig. 7a) revealed a six-fold decrease in the photoactivation rate in acidic media (pH 4.3) as compared to neutral, and only small rate changes at basic pH values (up to 9.0). The low pH-dependence of the activation rate is similar to previous observations on the protonation of the benzophenone triplet excited state[40,41], supporting the assumed involvement of this diradical in the activation mechanism. At high pH values, slow hydrolysis of **11-CF** was observed (Supplementary Fig. 7b); however, there was no difference in the absorption and emission spectra of **11-CF** and no change in product composition was detected by LC-MS up to pH 8.5 (Supplementary Fig. 7c), indicating little observable pH-sensitivity for this dye across the biologically relevant pH range. Furthermore, photoactivation of **11** proceeded cleanly in buffered solutions (pH 7) containing 2 mM mercaptoethylamine or glutathione (Supplementary Fig. 8), anticipating a lack of unwanted radical or electrophilic reactivity towards biomolecules, and a potential orthogonality with the single-molecule localization microscopy (SMLM) blinking buffers used for cyanine dyes[5]. Finally, we assessed the photostability of **11-CF**, benchmarking it against a series of commercially available

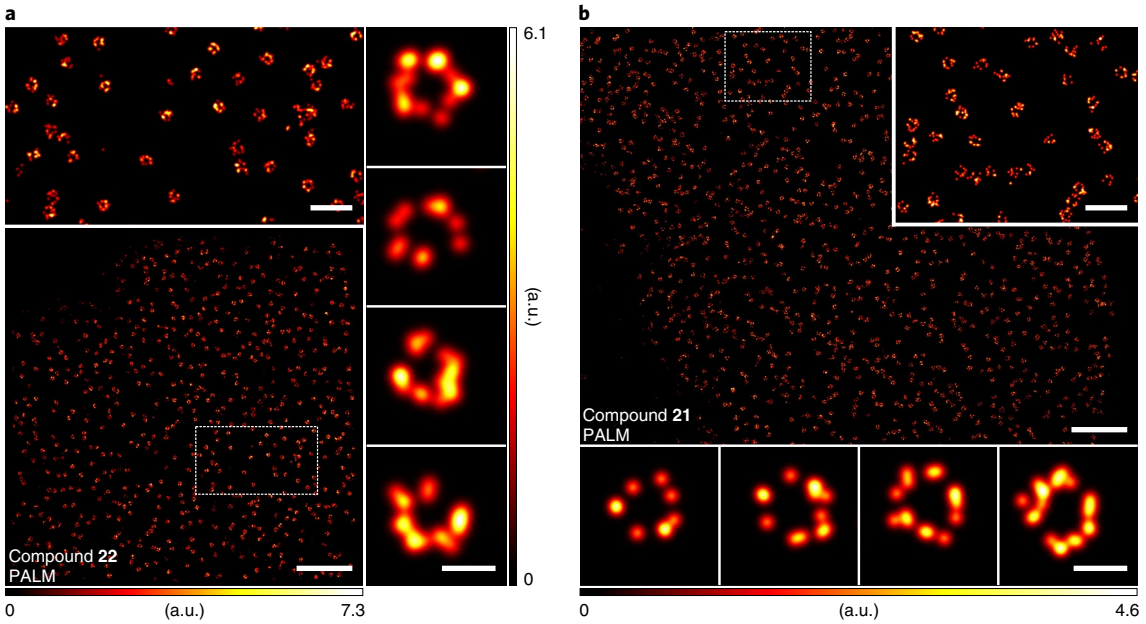

Fig. 5 | PALM imaging of NPCs in living cells using self-labelling PaX$_{560}$ substrates. a, Bottom: PALM image of U2OS stably expressing a NUP107–SNAP-tag construct labelled with **22**. Top: magnified view of the region marked in the overview image. Right column: magnified individual NPCs. **b**, Bottom: PALM image of U2OS cells stably expressing a NUP96-HaloTag construct labelled with **21**. Inset: magnified view of the region marked in the overview image. Bottom row: magnified individual NPCs. Scale bars: 2 µm (**a**,**b**, main), 500 nm (**a**,**b**, top insets), 100 nm (**a**, right column; **b**, bottom row).

dyes with similar spectral properties (Fig. 1h), and found that **11-CF** outperformed all of the tested fluorophores (for details, see Supplementary Information and Supplementary Figs. 9 and 10).

Caging-group-free photoactivatable labels for nanoscopy. Encouraged by the versatility of the PaX mechanism, we proceeded to construct targeted labels for fluorescence microscopy and nanoscopy. For indirect immunolabelling (with secondary antibodies or nanobodies), an amino-reactive *N*-hydroxysuccinimide (NHS) ester (**13**) and a thiol-reactive maleimide (**14**) derivative of PaX$_{560}$ were prepared (Fig. 2a), along with the NHS esters of PaX$_{480}$, PaX$_{525}$ and PaX+$_{560}$ (Supplementary Figs. 11a and 16–18). For actin labelling in fixed cells, a phalloidin derivative (**15**) of PaX$_{560}$ was assembled (Fig. 2a).

Thanks to their remarkable photo-fatigue resistance, we reasoned that PaX dyes would be strong candidates for STED imaging. We tested their performance by indirect immunofluorescence labelling of microtubules in fixed COS-7 cells. The fluorescent form of the dye was generated in situ (405-nm photoactivation) before STED imaging with 561-nm and 660-nm light for excitation and STED, respectively. Super-resolved images of microtubules were successfully acquired for antibody conjugates of PaX$_{560}$ (**13**; Fig. 2b), as well as of PaX$_{525}$ and PaX+$_{560}$ (**17**,**18**; Supplementary Fig. 11b), demonstrating their compatibility with STED nanoscopy. The specificity of PaX$_{560}$-phalloidin (**15**) for actin was validated in fixed neuron cultures in which the periodic membrane cytoskeleton structure of the axon was visualized by STED (Fig. 2c).

We next tested the performance of our photoactivatable labels in SMLM[42,43]. With this aim, PALM imaging was carried out on indirectly immunolabelled microtubules, and super-resolved images could be obtained for antibody conjugates bearing **13** (Fig. 2b) and **16**–**18** (Supplementary Fig. 11c). Thanks to the efficient photoactivation mechanism, very low powers (<100 µW) of activation light were required. Importantly, all samples were imaged in phosphate buffered saline (PBS) or in Mowiol, without the need for special blinking buffers or photostabilizing agents.

To further benchmark the utility of PaX labels for PALM imaging, indirect immunofluorescent labelling of nuclear pore complexes (NPCs) was conducted with a primary anti-NUP-98 antibody and secondary anti-rabbit nanobodies bearing **14** (Supplementary Fig. 12a,b). The PALM images of NPCs (Fig. 2d) were comparable in quality to those acquired through more demanding methods (for example, qPAINT[44]). Alternatively, the large-sized (~150 kDa) primary antibodies could be avoided to improve labelling precision[45] in cell lines expressing an mEGFP[46] (~27 kDa) fusion to NUP107 when combined with anti-GFP nanobodies labelled with **14** (Fig. 2e).

Targeted labels for live-cell imaging. To evaluate the compatibility of the PaX photoactivation mechanism with live imaging, we first prepared PaX$_{560}$ constructs (Fig. 3a) containing mitochondria-targeting triphenylphosphonium (**19**) and lysosome-targeting pepstatin A (**20**) moieties, as these selected organelles represent the extreme pH values found within the cell (pH 7.8 for the mitochondrial matrix and pH 4.5 in the lysosomal lumen). COS-7 cells were co-incubated with **19** and MitoTracker Deep Red and imaged with confocal microscopy before and after photoactivation with 355-nm light (Fig. 3b and Supplementary Video 1). The resulting fluorescence of **19-CF** co-localized strongly with the MitoTracker signal (Pearson correlation coefficient $r = 0.94$). Similarly, COS-7 cells concurrently labelled with the pepstatin A conjugate **20** and the lysosome-targeting fluorophore SiR-lysosome[20] demonstrated colocalization after photoactivation with $r = 0.84$. These results confirmed that the photoactivation mechanism is compatible with live-cell imaging in both high- and low-pH cellular environments.

Self-labelling protein tags, such as HaloTag and SNAP-tag, are well-established tools for targeting synthetic fluorophores to specific proteins in live-cell imaging[47]. Seeking to exploit this targeting strategy, we prepared the HaloTag-specific chloroalkane derivative (**21**) and the SNAP-tag specific O^6-benzylguanine derivative (**22**) of PaX$_{560}$ (Fig. 3a). Chloroalkane derivatives of PaX$_{480}$, PaX$_{525}$ and PaX+$_{560}$ were additionally prepared (Supplementary Figs. 13 and 23–25).

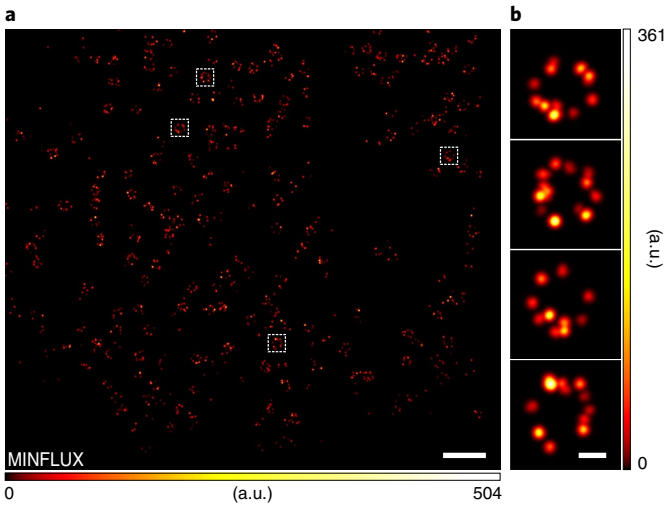

Fig. 6 | MINFLUX imaging of NPCs using PaX_{560}. a, MINFLUX image of NPCs in HeLa-Kyoto cells expressing NUP107-mEGFP labelled with anti-GFP nanobodies conjugated to **14**. **b**, Individual NPCs, as marked in **a**. Scale bars: 500 nm (**a**) and 50 nm (**b**).

Upon covalent linking of PaX_{560}-Halo (**21**) with the HaloTag protein, we observed a 7.8-fold increase in the photoactivation rate of the dye (Supplementary Fig. 14a–d). Complete reaction of **21** with HaloTag with only a slight excess (~1.1 equiv.) of the protein was confirmed by mass spectroscopy (Supplementary Fig. 14b,d). No major fluorescence intensity changes were observed for **21-CF** covalently bound to HaloTag in comparison to free **21-CF** in buffered solution (Supplementary Fig. 14e,f). However, a similar labelling efficiency and a greater fluorogenic response were observed upon binding of PaX_{560}–SNAP (**22**) to SNAP-tag, with an 11-fold increase in photoactivation rate (Supplementary Fig. 13a–d) and a 3.3-fold fluorescence intensity increase of SNAP-tag-bound **22-CF** in comparison to free **22-CF** (Supplementary Fig. 15e,f).

We then assessed the feasibility of two-photon activation of PaX_{560}–Halo (**21**) with 810-nm near-infrared (NIR) light, as shifting the excitation wavelength from UV to the NIR range reduces phototoxicity and increases imaging depth in tissues. U2OS cells stably expressing a vimentin–HaloTag fusion construct[48] were labelled with compound **21** and imaged with a confocal microscope equipped with a subpicosecond pulsed laser (Fig. 3c). The activation rate constant was determined for selected areas of the same sample by mono-exponential fitting of the activation rates measured with variable powers of a UV laser for one-photon activation (355 nm) or a subpicosecond pulsed laser for two-photon activation in the NIR (810 nm). Two-photon activation was confirmed by the nearly quadratic (1.84) dependence on the power of the excitation light (Fig. 3d). A pre-activated region of the same sample was further imaged using STED (at 660 nm) to resolve vimentin filaments with subdiffraction resolution, confirming that live-cell STED was readily possible with compound **21** (Fig. 3e). Live-cell STED time-lapse imaging further highlighted the cell dynamics after photoactivation (Supplementary Video 2).

Photoactivatable fluorophores can also be utilized together with regular 'always-active' fluorescent dyes having similar spectral properties for colour duplexing within a single excitation/detection channel, effectively doubling the number of available imaging channels in a confocal or STED system[12], provided that bleaching of the 'always-active' dye does not result in cell damage. To demonstrate this possibility with PaX labels, U2OS cells stably expressing a vimentin–HaloTag fusion protein were concurrently labelled with PaX_{560}–Halo (**21**) and an Abberior LIVE 560 tubulin (AL-560) probe, then imaged by confocal microscopy using a single detection channel (Fig. 4a–e). First, the AL-560-labelled tubulin filaments were visualized (Fig. 4a), followed by AL-560-photobleaching with high-intensity 560-nm excitation light (Fig. 4b). Compound **21** was then, in turn, photo-activated with a 405-nm laser to reveal the **21-CF**-labelled vimentin structure (Fig. 4c).

We explored the utility of the self-labelling protein tag substrates **21** and **22** for live-cell SMLM. U2OS cells stably expressing a SNAP-tag fusion with NUP107[49] were labelled with PaX_{560}–SNAP (**22**) and imaged with PALM (Fig. 5a). The reconstructed image shows largely complete circumferential labelling, which is remarkable given the one-to-one dye-to-protein ratio, highlighting the efficient labelling and efficient detection of activated PaX. Similarly, U2OS cells stably expressing HaloTag fusion proteins with NUP96[45] (another NPC protein) were labelled with PaX_{560}–Halo (**21**). The reconstructed image (Fig. 5b) resolved the structural elements of the NPCs with even greater efficiency. Fixation of live-labelled samples (with HaloTag and SNAP-tag fusion proteins) also allowed PALM imaging with similar contrast (Supplementary Fig. 16). Thus, the established fixation and permeabilization treatments used to preserve NUP structures[45] for super-resolution imaging do not affect the performance of PaX labels.

Multiplexing of PaX labels by selective photoactivation. Given the difference in photoactivation rates for the PaX dyes, we surmised that two complementary labels could be used for multiplexing purposes by sequentially applying a lower and a higher dose of activation light, to first convert one fluorophore (for example, PaX_{560}) while preserving the more difficult to activate (for example, PaX_{480}) until higher light doses are applied. We tested this first by confocal imaging (Supplementary Fig. 17a–e) and next by two-colour single-detector PALM imaging (Supplementary Fig. 17f) in fixed cells. We further demonstrated sequential activation in live cells (Supplementary Fig 18) by confocal imaging, using the organelle- (PaX_{560}–Mito **19** or PaX_{560}–Lyso **20**) and HaloTag-specific (PaX_{480}–Halo, **23**) labels.

Utilizing PaX labels in MINFLUX nanoscopy. Finally, we tested the PaX labels in MINFLUX nanoscopy[1,4], a recent technique that localizes individual fluorophores using an excitation beam with an intensity minimum (zero). Fixed HeLa-Kyoto cells expressing mEGFP fused to NUP107 were labelled with anti-GFP nanobodies bearing **14** and imaged by MINFLUX (Fig. 6a), yielding images of largely complete NPCs (Fig. 6b). On average, molecules were localized 106 times, utilizing 116 photons in the final MINFLUX iteration, and accounting for a mean label precision of 3.7 nm (s.d.).

Conclusion

We have introduced a general design strategy for caging-group-free, bright- and live-cell-compatible photoactivatable dyes, suitable for a wide range of optical microscopy and nanoscopy techniques, including PALM, STED and MINFLUX. The unique structural feature of these PaX dyes is the combination of a light-responsive 3,6-diaminoxanthone core functionalized with an intramolecular alkene radical trap, to give a highly compact and intrinsically uncharged, intact cell-membrane-permeable label. Under one- or two-photon activation, these compounds rapidly assemble into highly photostable fluorescent pyronine dyes. By changing the substitution pattern of PaX dyes, the photoactivation kinetics as well as the spectral properties can be tuned, allowing for both multiplexed pseudocolour as well as conventional multicolour imaging. The utility and versatility of PaX dyes is illustrated with a diverse range of target-specific probes and labelling strategies, for fixed- and live-cell super-resolution fluorescence microscopy experiments. We expect that our methodology will further stimulate the development of photoactivatable probes and sensors for biological imaging and material science. Further improvements to PaX fluorophores

will benefit applications in MINFLUX imaging and the recently proposed MINSTED nanoscopy[50].

Online content

Any methods, additional references, Nature Research reporting summaries, source data, extended data, supplementary information, acknowledgements, peer review information; details of author contributions and competing interests; and statements of data and code availability are available at https://doi.org/10.1038/s41557-022-00995-0.

Received: 1 October 2021; Accepted: 9 June 2022;
Published online: 21 July 2022

References

1. Schmidt, R. et al. MINFLUX nanometer-scale 3D imaging and microsecond-range tracking on a common fluorescence microscope. *Nat. Commun.* **12**, 1478 (2021).
2. Strauss, S. & Jungmann, R. Up to 100-fold speed-up and multiplexing in optimized DNA-PAINT. *Nat. Methods* **17**, 789–791 (2020).
3. Sahl, S. J., Hell, S. W. & Jakobs, S. Fluorescence nanoscopy in cell biology. *Nat. Rev. Mol. Cell Biol.* **18**, 685–701 (2017).
4. Balzarotti, F. et al. Nanometer resolution imaging and tracking of fluorescent molecules with minimal photon fluxes. *Science* **355**, 606–612 (2017).
5. Dempsey, G. T., Vaughan, J. C., Chen, K. H., Bates, M. & Zhuang, X. Evaluation of fluorophores for optimal performance in localization-based super-resolution imaging. *Nat. Methods* **8**, 1027–1036 (2011).
6. Hauke, S., von Appen, A., Quidwai, T., Ries, J. & Wombacher, R. Specific protein labeling with caged fluorophores for dual-color imaging and super-resolution microscopy in living cells. *Chem. Sci.* **8**, 559–566 (2017).
7. Grimm, J. B. et al. Synthesis of a far-red photoactivatable silicon-containing rhodamine for super-resolution microscopy. *Angew. Chem. Int. Ed.* **55**, 1723–1727 (2016).
8. Manley, S. et al. High-density mapping of single-molecule trajectories with photoactivated localization microscopy. *Nat. Methods* **5**, 155–157 (2008).
9. Grimm, J. B. et al. Bright photoactivatable fluorophores for single-molecule imaging. *Nat. Methods* **13**, 985–988 (2016).
10. Banaz, N., Makela, J. & Uphoff, S. Choosing the right label for single-molecule tracking in live bacteria: side-by-side comparison of photoactivatable fluorescent protein and Halo tag dyes. *J. Phys. D Appl. Phys.* **52**, 064002 (2019).
11. Jang, S., Kim, M. & Shim, S. H. Reductively caged, photoactivatable DNA-PAINT for high-throughput super-resolution microscopy. *Angew. Chem. Int. Ed.* **59**, 11758–11762 (2020).
12. Weber, M. et al. Photoactivatable fluorophore for stimulated emission depletion (STED) microscopy and bioconjugation technique for hydrophobic labels. *Chemistry* **27**, 451–458 (2021).
13. Lardon, N. et al. Systematic tuning of rhodamine spirocyclization for super-resolution microscopy. *J. Am. Chem. Soc.* **143**, 14592–14600 (2021).
14. Zheng, Q. et al. Rational design of fluorogenic and spontaneously blinking labels for super-resolution imaging. *ACS Cent. Sci.* **5**, 1602–1613 (2019).
15. Wang, L. et al. A general strategy to develop cell permeable and fluorogenic probes for multicolour nanoscopy. *Nat. Chem.* **12**, 165–172 (2020).
16. Bucevicius, J., Kostiuk, G., Gerasimaite, R., Gilat, T. & Lukinavicius, G. Enhancing the biocompatibility of rhodamine fluorescent probes by a neighbouring group effect. *Chem. Sci.* **11**, 7313–7323 (2020).
17. Grimm, J. B. et al. A general method to improve fluorophores using deuterated auxochromes. *JACS Au.* **1**, 690–696 (2021).
18. Grimm, J. B. et al. A general method to improve fluorophores for live-cell and single-molecule microscopy. *Nat. Methods* **12**, 244–250 (2015).
19. Koide, Y., Urano, Y., Hanaoka, K., Terai, T. & Nagano, T. Evolution of group 14 rhodamines as platforms for near-infrared fluorescence probes utilizing photoinduced electron transfer. *ACS Chem. Biol.* **6**, 600–608 (2011).
20. Lukinavicius, G. et al. Fluorogenic probes for multicolor imaging in living cells. *J. Am. Chem. Soc.* **138**, 9365–9368 (2016).
21. Butkevich, A. N. et al. Hydroxylated fluorescent dyes for live-cell labeling: synthesis, spectra and super-resolution STED. *Chemistry* **23**, 12114–12119 (2017).
22. Lukinavicius, G. et al. Fluorogenic probes for live-cell imaging of the cytoskeleton. *Nat. Methods* **11**, 731–733 (2014).
23. Lukinavicius, G. et al. A near-infrared fluorophore for live-cell super-resolution microscopy of cellular proteins. *Nat. Chem.* **5**, 132–139 (2013).
24. Wysocki, L. M. et al. Facile and general synthesis of photoactivatable xanthene dyes. *Angew. Chem. Int. Ed.* **50**, 11206–11209 (2011).
25. Grimm, J. B. et al. Carbofluoresceins and carborhodamines as scaffolds for high-contrast fluorogenic probes. *ACS Chem. Biol.* **8**, 1303–1310 (2013).
26. Zheng, Y. et al. Nitroso-caged rhodamine: a superior green light-activatable fluorophore for single-molecule localization super-resolution imaging. *Anal. Chem.* **93**, 7833–7842 (2021).
27. Belov, V. N., Wurm, C. A., Boyarskiy, V. P., Jakobs, S. & Hell, S. W. Rhodamines NN: a novel class of caged fluorescent dyes. *Angew. Chem. Int. Ed.* **49**, 3520–3523 (2010).
28. Halabi, E. A., Thiel, Z., Trapp, N., Pinotsi, D. & Rivera-Fuentes, P. A photoactivatable probe for super-resolution imaging of enzymatic activity in live cells. *J. Am. Chem. Soc.* **139**, 13200–13207 (2017).
29. Frei, M. S. et al. Photoactivation of silicon rhodamines via a light-induced protonation. *Nat. Commun.* **10**, 4580 (2019).
30. Irie, M. *Diarylethene Molecular Photoswitches*: *Concepts and Functionalities* (Wiley, 2021).
31. Ciamician, G. & Silber, P. Chemische Lichtwirkungen. *Ber. Dtsch. Chem. Ges.* **33**, 2911–2913 (2006).
32. Fagnoni, M. Modern molecular photochemistry of organic molecules. By Nicholas J. Turro, V. Ramamurthy and Juan C. Scaiano. *Angew. Chem. Int. Ed.* **49**, 6709–6710 (2010).
33. Dorman, G. & Prestwich, G. D. Benzophenone photophores in biochemistry. *Biochemistry* **33**, 5661–5673 (1994).
34. Horvath, P., Sebej, P., Solomek, T. & Klan, P. Small-molecule fluorophores with large Stokes shifts: 9-iminopyronin analogues as clickable tags. *J. Org. Chem.* **80**, 1299–1311 (2015).
35. Butkevich, A. N. et al. Fluorescent rhodamines and fluorogenic carbopyronines for super-resolution STED microscopy in living cells. *Angew. Chem. Int. Ed.* **55**, 3290–3294 (2016).
36. Butkevich, A. N., Lukinavicius, G., D'Este, E. & Hell, S. W. Cell-permeant large Stokes shift dyes for transfection-free multicolor nanoscopy. *J. Am. Chem. Soc.* **139**, 12378–12381 (2017).
37. Dell'Amico, L., Vega-Penaloza, A., Cuadros, S. & Melchiorre, P. Enantioselective organocatalytic Diels-Alder trapping of photochemically generated hydroxy-*o*-quinodimethanes. *Angew. Chem. Int. Ed.* **55**, 3313–3317 (2016).
38. Itoh, H., Kikuchi, T., Ishiyama, T. & Miyaura, N. Iridium-catalyzedortho-C–H borylation of aryl ketones with bis(pinacolato)diboron. *Chem. Lett.* **40**, 1007–1008 (2011).
39. Zhou, D., Chu, W., Voller, T. & Katzenellenbogen, J. A. Copper-mediated nucleophilic radiobromination of aryl boron precursors: convenient preparation of a radiobrominated PARP-1 inhibitor. *Tetrahedron Lett.* **59**, 1963–1967 (2018).
40. Shizuka, H. & Kimura, E. Acid-base properties in the triplet-state of aromatic ketones studied by nanosecond laser flash-photolysis. *Can. J. Chem.* **62**, 2041–2046 (1984).
41. Ramseier, M., Senn, P. & Wirz, J. Photohydration of benzophenone in aqueous acid. *J. Phys. Chem. A* **107**, 3305–3315 (2003).
42. Sauer, M. & Heilemann, M. Single-molecule localization microscopy in eukaryotes. *Chem. Rev.* **117**, 7478–7509 (2017).
43. Li, H. & Vaughan, J. C. Switchable fluorophores for single-molecule localization microscopy. *Chem. Rev.* **118**, 9412–9454 (2018).
44. Jungmann, R. et al. Quantitative super-resolution imaging with qPAINT. *Nat. Methods* **13**, 439–442 (2016).
45. Thevathasan, J. V. et al. Nuclear pores as versatile reference standards for quantitative superresolution microscopy. *Nat. Methods* **16**, 1045–1053 (2019).
46. Otsuka, S. et al. Nuclear pore assembly proceeds by an inside-out extrusion of the nuclear envelope. *eLife* **5**, e19071 (2016).
47. Xue, L., Karpenko, I. A., Hiblot, J. & Johnsson, K. Imaging and manipulating proteins in live cells through covalent labeling. *Nat. Chem. Biol.* **11**, 917–923 (2015).
48. Butkevich, A. N. et al. Two-color 810-nm STED nanoscopy of living cells with endogenous SNAP-tagged fusion proteins. *ACS Chem. Biol.* **13**, 475–480 (2018).
49. Li, Y. et al. Real-time 3D single-molecule localization using experimental point spread functions. *Nat. Methods* **15**, 367–369 (2018).
50. Weber, M. et al. MINSTED fluorescence localization and nanoscopy. *Nat. Photon.* **15**, 361–366 (2021).

Methods

Detailed procedures for the synthesis of all compounds and their characterizations, as well as methods sample preparation, live and fixed-cell labelling for microscopy and nanoscopy, are provided in the Supplementary Information. Image acquisition conditions for confocal and STED (Supplementary Table 3) and PALM (Supplementary Table 4), as well as detailed procedures for image processing and rendering, are provided in the Supplementary Information.

Statistics and reproducibility. All biochemical or spectroscopic data were obtained in triplicate with similar results. All staining/labelling of cells was performed in triplicate. Cells for microscopy were selected at random during the imaging session; sufficient microscopy images were collected, from experience, to ensure their representation of the sample.

Cell culture. COS-7, HeLa, U2OS-Vim-Halo, U2OS-Vim-SNAP[48,51] and HK-2xZFN-mEGFP-Nup107[46] cells were cultured in Dulbecco's modified Eagle medium (DMEM, 4.5 g l^{-1} glucose) containing GlutaMAX and sodium pyruvate (ThermoFisher 31966), supplemented with 10% (vol/vol) fetal bovine serum (FBS, ThermoFisher 10500064) and 1% Pen Strep (GIBCO, 15140122) in a humidified 5% CO_2 incubator at 37 °C. Cells were split every 2–4 days or at confluency, and were regularly tested for mycoplasma contamination.

U2OS-ZFN-SNAP-Nup107[49] and U2OS-NUP96-Halo[45] cells were cultured in McCoy's 5a (modified) medium (GIBCO, 26600023) containing L-glutamine and sodium pyruvate, supplemented with 10% (vol/vol) FBS and 1% Pen Strep (GIBCO, 15140122) in a humidified 5% CO_2 incubator at 37 °C. Cells were split every 2–4 days or at confluency, and were regularly tested to ensure no mycoplasma contamination.

Cell lines with genetically introduced self-labelling tags were verified by confocal microscopy using previously reported fluorophore labels.

Neuronal culture preparation and labelling. Cultures of dissociated rat hippocampal primary neurons were prepared from postnatal P0-P1 Wistar rats of either sex and cultured on glass coverslips coated with 100 µg ml^{-1} poly-ornithine (Merck KGaA) and 1 µg ml^{-1} laminin (BD Biosciences). Procedures were performed in accordance with the Animal Welfare Act of the Federal Republic of Germany (Tierschutzgesetz der Bundesrepublik Deutschland, TierSchG) and the Animal Welfare Laboratory Animal Regulations (Tierschutzversuchsverordnung). According to the TierSchG and the Tierschutzversuchsverordnung, no ethical approval from the ethics committee is required for the procedure of euthanizing rodents for subsequent extraction of tissues. The procedure for euthanizing P0-P1 rats performed in this study was supervised by animal welfare officers of the Max Planck Institute for Medical Research (MPImF) and conducted and documented according to the guidelines of the TierSchG (permit number assigned by the MPImF: MPI/T-35/18).

Cells were grown in the presence of 1-β-D-arabinofuranosyl-cytosin (Merck KGaA) at 37 °C and 5% CO_2. Cultures were fixed at 27 days in vitro in 4% paraformaldehyde in PBS, pH 7.4 for 20 min, and quenched for 5 min in PBS supplemented with 100 mM glycine and 100 mM ammonium chloride. Cells were permeabilized for 5 min in 0.1% Triton X-100, blocked with 1% bovine serum albumin for 30 min and incubated with 1 µM **15** diluted in PBS. After extensive washing in PBS, samples were mounted in Mowiol supplemented with DABCO. The identification of axons was facilitated by staining of the axon initial segment with an anti-neurofascin primary antibody (NeuroMab, cat. no. 75-172) and an anti-mouse STAR GREEN (Abberior, cat. no. STGREEN-1001) secondary antibody.

Reporting summary. Further information on research design is available in the Nature Research Reporting Summary linked to this Article.

Data availability

The data supporting the findings of this study are provided within the Paper and its Supplementary Information. The data are also available from the corresponding authors upon reasonable request. Source data are provided with this Paper.

Code availability

The custom code used for image rendering is available at https://github.com/mbossi2015/paper_PaX.

References

51. Ratz, M., Testa, I., Hell, S. W. & Jakobs, S. CRISPR/Cas9-mediated endogenous protein tagging for RESOLFT super-resolution microscopy of living human cells. *Sci. Rep.* **5**, 9592 (2015).

Acknowledgements

The research was funded by Bundesministerium für Bildung und Forschung (German Federal Ministry of Education and Research), project no. 13N14122 '3D Nano Life Cell' (S.W.H.). R.L. is grateful to the Max Planck Society for a Nobel Laureate Fellowship. We thank S. Jakobs (MPI-NAT) for providing the U2OS-Vim-Halo and U2OS-Vim-SNAP cells and the EMBL for providing the U2OS-ZFN-SNAP-Nup107, U2OS-NUP96-Halo and HK-2xZFN-mEGFP-Nup107 cells. We thank the following people at the MPI for Medical Research: S. Fabritz (Mass Spectrometry Core Facility) for recording mass spectra of proteins and small molecules, M. Steigleder (Electronics Workshop) for building the custom 405-nm light source for the Penn m1 photoreactor, K. Johnsson (Department of Chemical Biology) for the SNAP-tag protein, M. Tarnawski (Protein Expression and Characterization Facility) for the HaloTag7 protein, and our colleagues at the Department of Optical Nanoscopy—J. Hubrich for supporting the cell culture, A. Aktalay for assistance with labelling of nanobody samples, and J. Matthias for critical reading of the manuscript and advice on sample preparation for MINFLUX. We thank the team at Abberior Instruments for support on the MINFLUX image acquisition.

Author contributions

R.L. was responsible for the project's conception and wrote the manuscript with input from A.N.B., M.L.B. and S.W.H. A.N.B. designed and validated the synthetic routes. A.N.B. and R.L. performed the chemical synthesis. M.L.B. and R.L. performed dye characterization and mechanistic studies. M.L.B. and M.R. performed labelling, STED, PALM, MINFLUX microscopy and data analysis. E.D. performed the live-cell STED time-lapse imaging and culture, labelling, microscopy and data analysis of the primary neurons. S.W.H. directed and supervised the investigations. All the authors discussed the results and commented on the manuscript.

Funding

Open access funding provided by Max Planck Society.

Competing interests

The authors declare the following competing financial interest(s): R.L., M.L.B. and A.N.B. are co-inventors of a patent application (International Patent Application No. PCT/EP2021/069804) covering the photoactivatable dyes of this work, filed by the Max Planck Society. S.W.H. owns shares of Abberior GmbH and Abberior Instruments GmbH, whose dyes and MINFLUX microscope, respectively, have been used in this study. The remaining authors declare no competing interests.

Additional information

Supplementary information The online version contains supplementary material available at https://doi.org/10.1038/s41557-022-00995-0.

Correspondence and requests for materials should be addressed to Alexey N. Butkevich or Stefan W. Hell.

Peer review information *Nature Chemistry* thanks Francisco Raymo and the other, anonymous, reviewer(s) for their contribution to the peer review of this work.

Reprints and permissions information is available at www.nature.com/reprints.

nature portfolio

Corresponding author(s): Dr. Alexey N. Butkevich
Prof. Dr. Stefan W. Hell

Last updated by author(s): Apr 18, 2022

Reporting Summary

Nature Portfolio wishes to improve the reproducibility of the work that we publish. This form provides structure for consistency and transparency in reporting. For further information on Nature Portfolio policies, see our Editorial Policies and the Editorial Policy Checklist.

Statistics

For all statistical analyses, confirm that the following items are present in the figure legend, table legend, main text, or Methods section.

n/a	Confirmed
☒	☐ The exact sample size (*n*) for each experimental group/condition, given as a discrete number and unit of measurement
☒	☐ A statement on whether measurements were taken from distinct samples or whether the same sample was measured repeatedly
☒	☐ The statistical test(s) used AND whether they are one- or two-sided *Only common tests should be described solely by name; describe more complex techniques in the Methods section.*
☒	☐ A description of all covariates tested
☒	☐ A description of any assumptions or corrections, such as tests of normality and adjustment for multiple comparisons
☒	☐ A full description of the statistical parameters including central tendency (e.g. means) or other basic estimates (e.g. regression coefficient) AND variation (e.g. standard deviation) or associated estimates of uncertainty (e.g. confidence intervals)
☒	☐ For null hypothesis testing, the test statistic (e.g. *F*, *t*, *r*) with confidence intervals, effect sizes, degrees of freedom and *P* value noted *Give P values as exact values whenever suitable.*
☒	☐ For Bayesian analysis, information on the choice of priors and Markov chain Monte Carlo settings
☒	☐ For hierarchical and complex designs, identification of the appropriate level for tests and full reporting of outcomes
☐	☒ Estimates of effect sizes (e.g. Cohen's *d*, Pearson's *r*), indicating how they were calculated

Our web collection on statistics for biologists contains articles on many of the points above.

Software and code

Policy information about availability of computer code

Data collection	Bruker Topspin 3.5, LabSolutions 5.89, Cary Eclipse Scan Application 1.2(147), Cary Eclipse WinUV Scan Application 6.2.0.1588, MatLab R2007a, Imspector (16.1.6905, 16.3.13033, 16.3.13367), LabVIEW 2019 32bit, Andor Solis 4.31.30022, EasyTau 1.4
Data analysis	MestReNova 11.0.3, Imspector (16.1.6905, 16.3.13033, 16.3.13367), ImageJ 1.52i, ImageJ 1.53f51, OriginPro 2020 (64-bit) SR1 9.7.0.188, MatLab R2007a, FluoFit 4.6.6.0

For manuscripts utilizing custom algorithms or software that are central to the research but not yet described in published literature, software must be made available to editors and reviewers. We strongly encourage code deposition in a community repository (e.g. GitHub). See the Nature Portfolio guidelines for submitting code & software for further information.

Data

Policy information about availability of data

All manuscripts must include a data availability statement. This statement should provide the following information, where applicable:

- Accession codes, unique identifiers, or web links for publicly available datasets
- A description of any restrictions on data availability
- For clinical datasets or third party data, please ensure that the statement adheres to our policy

The data supporting the findings of this study are available within the paper and its Supplementary Information and are available from the corresponding author upon reasonable request.

Field-specific reporting

Please select the one below that is the best fit for your research. If you are not sure, read the appropriate sections before making your selection.

☒ Life sciences ☐ Behavioural & social sciences ☐ Ecological, evolutionary & environmental sciences

For a reference copy of the document with all sections, see nature.com/documents/nr-reporting-summary-flat.pdf

Life sciences study design

All studies must disclose on these points even when the disclosure is negative.

Sample size	No sample-size calculation was performed as no biologically-relevant outcome was analyzed. Sufficient microscopy images were collected from experience to ensure their representation of the sample.
Data exclusions	No data were excluded.
Replication	All biochemical or spectroscopic data was performed in triplicate with similar results. All staining/labelling of cells was performed in triplicate.
Randomization	No randomizations were required for the experiments performed. Control of covariates was not relevant to the study as no biologically-relevant outcome was analyzed. Cells for microscopy were selected at random during the imaging session.
Blinding	No blinding was required for the experiments performed as no biologically-relevant outcome was analyzed.

Reporting for specific materials, systems and methods

We require information from authors about some types of materials, experimental systems and methods used in many studies. Here, indicate whether each material, system or method listed is relevant to your study. If you are not sure if a list item applies to your research, read the appropriate section before selecting a response.

Materials & experimental systems

n/a	Involved in the study
☐	☒ Antibodies
☐	☒ Eukaryotic cell lines
☒	☐ Palaeontology and archaeology
☐	☒ Animals and other organisms
☒	☐ Human research participants
☒	☐ Clinical data
☒	☐ Dual use research of concern

Methods

n/a	Involved in the study
☒	☐ ChIP-seq
☒	☐ Flow cytometry
☒	☐ MRI-based neuroimaging

Antibodies

Antibodies used	AffiniPure Goat Anti-Rabbit IgG (H+L), Goat, Jackson ImmunoResearch Europe Ltd., 111-005-003 AffiniPure Goat Anti-Mouse IgG (H+L), Goat, Jackson ImmunoResearch Europe Ltd., 115-005-003 sdAB anti-Mouse kappa light chain (kLC), unconjugated, Camelid, NanoTag Biotechnologies, N1202 sdAb anti-Rabbit IgG, unconjugated, Camelid, NanoTag Biotechnologies, N2402 FluoTag-X2 anti-GFP unconjugated clone 1H, Camelid, NanoTag Biotechnologies, N0302 FluoTag-X2 anti-GFP unconjugated clone 1B, Camelid, NanoTag Biotechnologies, N0303 Pan-Neurofascin (extracellular), Mouse, Neuromab, 75-172 abberior STAR GREEN, goat anti-mouse IgG, Goat, Abberior, STGREEN-1001 Anti-Clathrin heavy chain antibody, Rabbit, Abcam, ab21679 Anti-Nup153 antibody [QE5], Mouse, Abcam, ab24700 alpha-Tubulin antibody, Mouse, Synaptic Systems, 302 211 NUP98 (C39A3) Rabbit mAb, Rabbit, Cell Signalling, #2598
Validation	antibodies and nanobodies were used without further validation as the obtained labelling was clearly compatible with the expected structures. All reagents have already been extensively used by us and others. FFluoTag-X2 anti-GFP unconjugated clone 1H, Camelid, NanoTag Biotechnologies, N0302: Manufacturer reports “Recognizes GFP (green fluorescent protein) and common GFP derivatives like EGFP, mEGFP, Sirius, tSapphire, Cerulean, eCFP, mTurquoise, acGFP, Emerald, superecliptic pHluorin, paGFP, superfolder GFP, eYFP, mVenus and Citrine.” utilization in Immunofluorescence (https://nano-tag.com/product/fluotag-x4-anti-gfp/). FluoTag-X2 anti-GFP unconjugated clone 1B, Camelid, NanoTag Biotechnologies, N0303: Manufacturer reports “Recognizes GFP (green fluorescent protein) and common GFP derivatives like EGFP, mEGFP, Sirius, tSapphire, Cerulean, eCFP, mTurquoise, acGFP, Emerald, superecliptic pHluorin, paGFP, superfolder GFP, eYFP, mVenus and Citrine.” utilization in Immunofluorescence (https://

nano-tag.com/product/fluotag-x4-anti-gfp/).
Pan-Neurofascin (extracellular), Mouse, Neuromab, 75-172: Utilized for western blot, immunohistochemistry, immunocytochemistry; reported in 30 references (https://www.labome.com/product/Neuromab/75-172.html).
Anti-Clathrin heavy chain antibody, Rabbit, Abcam, ab21679: Manufacturer reports "confirmed specificity through extensive validation"; utilized in Western blot and Immunocytochemistry; reported in 114 references (https://www.abcam.com/clathrin-heavy-chain-antibody-ab21679.html).
Anti-Nup153 antibody [QE5], Mouse, Abcam, ab24700: Manufacturer reports "ab24700 could also recognise other NPC polypeptides, p250 and p62, apart from Nup153."; utilization in Immunocytochemistry/Immunofluorescence; reported in 50 references (https://www.abcam.com/nup153-antibody-qe5-ab24700.html).
alpha-Tubulin antibody, Mouse, Synaptic Systems, 302 211: Manufacturer reports "Specific for α-tubulin (glu- and tyr-α-tubulin)"; utilization in Western blot and Immunocytochemistry; reported in 14 references (https://sysy.com/product/302211).
NUP98 (C39A3) Rabbit mAb, Rabbit, Cell Signalling, #2598: Manufacturer reports "NUP98 (C39A3) Rabbit mAb detects endogenous levels of total NUP98 protein"; utilization in Western blot and Immunofluorescence; reported in 37 references (https://www.cellsignal.de/products/primary-antibodies/nup98-c39a3-rabbit-mab/2598).

Eukaryotic cell lines

Policy information about cell lines

Cell line source(s)	COS-7, Hölzl Biotech, AddexBio (T0014002); HeLa, Kräusslich Group, Virology, University Heidelberg; U2OS-Vim-Halo, Jakobs Group, Structure & Dynamics of Mitochondria, MPI Multidisciplinary Sciences; U2OS-Vim-SNAP, Jakobs Group, Structure & Dynamics of Mitochondria, MPI Multidisciplinary Sciences; HK-2xZFN-mEGFP-Nup107, CLS Cell Lines Service GmbH (300676); U2OS-ZFN-SNAP-Nup107; CLS Cell Lines Service GmbH (300294); U2OS-NUP96-Halo, CLS Cell Lines Service GmbH (300448).
Authentication	The cell lines were used without further authentication. Genetically modified cells lines clearly exhibited the expected labeling pattern.
Mycoplasma contamination	Cell lines were regularly tested for mycoplasma contamination and were negative. Primary neuron cultures were not tested.
Commonly misidentified lines (See ICLAC register)	Not applicable as no commonly misidentified cell lines were used.

Animals and other organisms

Policy information about studies involving animals; ARRIVE guidelines recommended for reporting animal research

Laboratory animals	Postnatal day 0-1 Wistar rats of either sex.
Wild animals	The study did not involve wild animals.
Field-collected samples	The study did not involve samples collected from the field.
Ethics oversight	Procedures were performed in accordance with the Animal Welfare Act of the Federal Republic of Germany (Tierschutzgesetz der Bundesrepublik Deutschland, TierSchG) and the Animal Welfare Laboratory Animal Regulations (Tierschutzversuchsverordnung). According to the TierSchG and the Tierschutzversuchsverordnung no ethical approval from the ethics committee is required for the procedure of sacrificing rodents for subsequent extraction of tissues, as performed in this study. The procedure for sacrificing P0–P2 rats performed in this study was supervised by animal welfare officers of the Max Planck Institute for Medical Research (MPImF) and conducted and documented according to the guidelines of the TierSchG (permit number assigned by the MPImF: MPI/T-35/18).

Note that full information on the approval of the study protocol must also be provided in the manuscript.